Autonomous Suturing Framework and Quantification Using a Cable-Driven Surgical Robot

Sahba Aghajani Pedram ⓘ, *Member, IEEE*, Changyeob Shin ⓘ, *Member, IEEE*, Peter Walker Ferguson ⓘ, *Graduate Student Member, IEEE*, Ji Ma ⓘ, Erik P. Dutson, and Jacob Rosen, *Member, IEEE*

Abstract—Suturing is required in almost all surgeries but it is challenging to perform with surgical robots due to limited vision and/or haptic feedback. To tackle this problem, we present an autonomous suturing framework that encompasses a novel needle path planner, as well as an accurate needle pose estimator and a six degrees-of-freedom controller. A novel needle grasper is developed that enables needle pose estimation both inside and outside the tissue. The framework was evaluated experimentally using the Raven IV surgical system and important suture parameters were quantified. The experiment results confirmed a needle pose estimation accuracy of < 0.87 mm in position and $< 3.46°$ in orientation across all directions. Moreover, the results revealed that using the proposed framework enabled following the reference needle trajectories with errors of 2.07 mm in position and 4.29° in orientation. These are drastic improvements of more than $10\times$ in position and $5\times$ in orientation compared to the Raven IV kinematic controller. Additionally, the results verified that our framework delivered the desired clinical suture parameters successfully across tissue phantom environments with different mechanical properties and under various needle trajectories. A supplementary video can be found at: http://bionics.seas.ucla.edu/research/surgeryproject18.htmlhttp://bionics.seas.ucla.edu/research/surgeryproject18

Index Terms—Autonomous surgical robotics, intelligent robotic surgery, Raven surgical robot, robot-assisted surgery, suturing automation.

I. Introduction

TELEOPERATED robotic surgery systems enable surgeons to perform surgical procedures with enhanced three-dimensional (3-D) vision and ergonomics, intuitive hand–eye coordination, and small-scale motion. However, there is a fundamental factor limiting the utility gained from these systems. Surgeons are fully responsible for both decision making and action execution while robots merely follow surgeon's commands. Although the surgeon is indispensable for decision making as they have a more complete understanding of the operational requirements, they have limited sensing and action capabilities. Muscle fatigue, restricted sensing capacities, and confined motion dexterity are the key limiting factors [1]. Due to this limitation and the continued growth of machine capabilities, robot autonomy has been introduced into surgical robotics [2].

Current teleoperated robotic systems for soft tissue surgeries, such as da Vinci [3] and Raven [4] (see Fig. 1), are cable driven, which allows remote placement of motors to reduce manipulator size, mass, and inertia on the arms. Despite the great advantages, cable-driven design results in a large positioning error due to elasticity of cables and long kinematic chains of the robotic systems [5]. For teleoperated systems, surgeons compensate for such errors using direct visual feedback of the surgical scenes. Incorporating robot autonomy into soft tissue surgery, however, requires high positioning accuracy and hence enhanced solutions are required for the current surgical robots.

Surgical subtask automation is midlevel autonomy in surgical robotics [2]. Suturing is one of the most challenging and time consuming of all surgical subtasks [6]. Compared to open surgery, suturing using surgical robots is even more difficult due to limited vision and/or haptic feedback [7]. This can cause complications, such as increased tissue trauma from multiple attempts to extract the needle [8] or suture breakage due to lack of force feedback [7]. These challenges, along with the repetitive nature of suturing, make this subtask a great candidate for automation. Suturing can be decomposed into the following seven steps:

   (I) grasping the needle with the inserting arm;
  (II) moving toward the wound and entering the tissue perpendicularly;
 (III) stitching;
 (IV) grasping the needle with the extracting arm;
  (V) extracting needle;
 (VI) knot tying and grasping the needle with the extracting arm;
(VII) handing off the needle to the inserting arm.

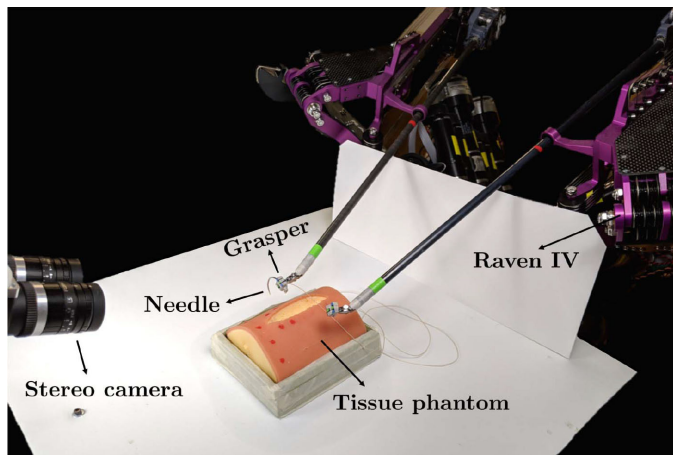In this article, we consider automating steps (II)–(V) and (VII).

Fig. 1.   Experiment setup of bimanual autonomous suturing.

In recent years, robot autonomy has been applied to surgical subtasks, such as tissue manipulation [9]–[12], tissue cutting [13], tumor localization [14], and, in particular, suturing. In [15], optimal needle grasp and entry point were selected based on metrics, such as robot dexterity to perform suturing. Shademan *et al.* [16] reported a series of autonomous robot-assisted tasks, such as linear suturing and end-to-end anastomosis in *ex vivo* and *in vivo* settings. A robotic suturing framework that deployed the kinematic relationship between needle and robot base to servo the RAVEN surgical robot is presented in [17]. In [18], an optimization-based needle path planning was proposed and implemented with the da Vinci Research Kit using robot kinematics and camera registration. Staub *et al.* [19] presented image-based visual servoing for stitching automation but did not consider factors such as suture depth and a possible needle slip. A single Denso robot arm and monocular camera system was proposed for suturing automation in [20]. In [21] and [22], a needle stitching planner and a 2-D vision-based path following method were proposed to perform automated stitching using a 4-DoF surgical robotic arm with no articulating wrist. Jackson and Çavuşoğlu [23] suggested two stitching algorithms for autonomous stitching that were executed with an ABB robot arm in an open-loop fashion (e.g., no external sensor such as vision). A customized suturing tool to guide the needle was installed on a KUKA robot and used to automate suturing [24]. Huang *et al.* [25] developed a multirobot framework that used human demonstrations, a vision-based controller, and KUKA robots for sewing stent grafts, which is analogous to surgical suturing. Hu *et al.* introduced a customized sewing device and implemented autonomous sewing with an ABB robot [26].

While these studies provided valuable insights into suturing automation, they have notable limitations. First, it is important to quantify suturing related parameters (e.g., tissue trauma) to assess the performance of an autonomous algorithm. However, the only parameters quantified in any studies were suture spacing and leaked pressure in [16], interaction force/torque in [23], and

stitch size in [25]. Second, the estimation of needle pose in most of these studies (e.g. [19]) was obtained with an assumption that no needle slip occurs, which is not realistic. Third, some studies developed estimation and control methods for nonarticulated wrists [22], [25] or custom-built suturing devices [16], which are not directly applicable to surgical robots with articulated instruments. Fourth, studies such as in [16], [18], and [20] relied on robot kinematics and camera registration for servoing, which, as discussed, can be inaccurate for cable-driven systems. Finally, none of the studies evaluated their algorithms on environments with different tissue properties, therefore, it is questionable if the performance is consistent across environments.

Contributions. We have previously formulated needle stitching path planning as a nonlinear optimization problem, which outputs the optimal position of the needle center as well as the needle size and shape [27]. To extend this work and overcome the shortcomings of the previous autonomous suturing studies, we propose a framework with enhanced hardware and software solutions. Namely, the main contributions of this article are as follows.

(1) Comprehensive quantification of suture parameters under autonomous robotic suturing.
(2) Solutions for accurate 6-DoF servoing of a cable-driven surgical robotic system.
(3) Robust pose estimation of a suture needle grasped by an articulated robotic arm throughout all suturing steps.
(4) Implementation and verification of a novel needle path planning algorithm with robotic bimanual operation.
(5) Evaluation of performance under different suturing criteria and with different types of tissue.

II. METHOD

To automate suturing with a cable-driven surgical robot, a needle stitching path planning algorithm as well as enhanced hardware and software solutions is developed. First, the notations and coordinate frames used throughout this article are defined. Afterward, the needle path planning algorithm is presented. Finally, a vision-based controller, enhanced hardware solutions, and computer vision algorithms are detailed.

A. Notations and Definitions

We use $^j\bullet_i$ to define information of frame i as presented in frame j. We use $\bullet^{\text{err}}$, $\bullet^{\text{des}}$, and $\hat{\bullet}$ to refer to error, desired, and estimated values. We represent rigid motions and rotations by the special Euclidean group $\text{SE}(n)$ and the special orthogonal group $\text{SO}(n)$ in dimension n. The *needle shape* is the arc length of the needle divided by ($\pi \times$needle diameter). We denote an identity matrix $\in \mathbb{R}^{n \times n}$ as $\mathbf{I}_n$, and zero and one matrices $\in \mathbb{R}^{m \times n}$ as $\mathbf{0}_{m \times n}$ and $\mathbf{1}_{m \times n}$, respectively. We use $\overrightarrow{A}$, $\overrightarrow{A}_x$, and $\overrightarrow{A}_y$ to refer to vector A and its x and y components, respectively. We use $\otimes$ for Kronecker matrix product operator.

There are a total of seven frames defined to address the autonomous suturing (see Fig. 2): *camera* (C), *robot base* (B),
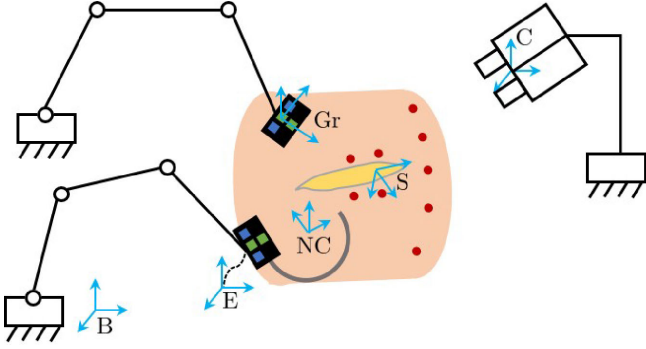
Fig. 2.   Schematic of the autonomous suturing setup. Blue arrows represent frames, the pink object represents tissue, the yellow part represents wound, and the four red dots surrounding the wound represent desired entry/exit points. The other five red dots are used to find the tissue angle.

robot end-effector (E), *grasper* (Gr), *needle center* (NC), and *stitch* (S) frames.

B. Needle Path Planning Algorithm

One of the main pillars of an automated suturing framework is stitching planning, which deals with optimal motion of the needle inside the tissue based on clinical criteria. Examples of such criteria [28] are: entering the tissue perpendicularly; reaching specific suture depth; and minimizing tissue trauma. Here, our previous work on stitching planning [27] that was formulated based on such criteria is summarized as follows.

All needle motions can be categorized as either fixed center motion (FCM) or moving center motion (MCM) [27]. In FCM, the needle tip position changes by merely rotating the needle around its geometrical center. In MCM, however, the position of the needle tip changes by rotating the needle around any point except its center. In this article, we deploy FCM as it is encouraged in the context of surgical suturing and is associated with minimal tissue trauma [8]. The drawback of this method, however, is that it constrains the motion of the needle in which some important suturing criteria such as suture depth might not be met. We address this by formulating a constrained nonlinear optimization to satisfy a number of important suturing criteria.

Assumptions: Because FCM ideally creates only small shear forces, it is assumed that interaction forces between needle and tissue can be neglected as in [19] and [29]. With this assumption, the needle path planning can be formulated as a kinematics problem. As in ideal FCM, motion of the needle is restricted to be planar. Tissue geometry can be approximated as in Fig. 3 , with surgeons specifying I_d and O_d.

Based on the suturing guidelines [30], we define $\mathbf{r}_s = [\beta_{\text{in}}, e_{\text{in}}, d_h, s_n, \beta_{\text{out}}, e_{\text{out}}]^\mathsf{T} \in \mathbb{R}^6$ as a vector of suture parameters, which fully quantifies a suture. The needle parameters vector is defined as $\mathbf{r}_n = [s_0, l_0, d_c, a_n]^\mathsf{T} \in \mathbb{R}^4$. All the variables of the needle path planning are defined in Table I.

From kinematics analysis of Fig. 3 (details are provided in [27]), a nonlinear function $\Phi : \mathbb{R}^4 \to \mathbb{R}^6$ that maps needle parameters to suture parameters $(\mathbf{r}_s = \Phi(\mathbf{r}_n))$ is defined as

TABLE I
DEFINITION OF VARIABLES (ALPHABETICALLY SORTED)

Var.	Definition	Var.	Definition
a_n	Needle shape	M	Deepest point of needle
b	Distance between I_d and E_i	O_a	Actual needle exit point
C_0	Needle's geometric center	O_d	Desired needle exit point
d_h	Suture depth	P	Tip of the needle
d_c	Needle's diameter	Q	Rear end of the needle
e_{in}	Distance between I_a and I_d	s_0	x position of C_0
e_{out}	Distance between O_a and O_d	s_n	Suture symmetry
E_i	Edge of wound on entry side	w_w	Wound width
E_O	Edge of wound on exit side	W_b	Bottom edge of the wound
h_{ti}	Predefined needle-tissue distance	W_t	Top edge of the wound
I_a	Actual needle entry point	α_1	Angle between $E_o O_a$
I_d	Desired needle entry point		and $C_o O_a$
l_g	Length of the needle out of	α_2	Angle between $E_i I_a$
	the tissue		and $C_o I_a$
l_{ins}	Min. length of needle the	β_{out}	Exit angle
	instrument can grasp	β_{in}	Entry angle
l_{io}	Distance between I_d and O_d	γ	Tissue angle
l_0	y position of C_0	ξ_i	Optimization coefficients

follows:

$$\beta_{in} = \frac{\pi}{2} + \alpha_2, \, \beta_{\text{out}} = \frac{\pi}{2} + \alpha_1$$

$$d_h = \left| -\frac{d_c}{2} + l_0 - b\sin(\frac{\pi - \gamma}{2}) \right|, s_n = |s_0|$$

$$e_{\text{in}} = \frac{-\frac{d_c}{2}\cos\left(\alpha_2 + \frac{\pi-\gamma}{2}\right) + \frac{l_{io}}{2} - s_0}{\cos\left(\frac{\pi-\gamma}{2}\right)}$$

$$e_{\text{out}} = \frac{-\frac{d_c}{2}\cos\left(\alpha_1 + \frac{\pi-\gamma}{2}\right) + \frac{l_{io}}{2} + s_0}{\cos\left(\frac{\pi-\gamma}{2}\right)}$$

$$\alpha_i = \sin^{-1}\left(\frac{2\sin(\frac{\gamma}{2})}{d_c}(l_0 - \tan(\frac{\pi - \gamma}{2})(\frac{l_{io}}{2} + (-1)^{i+1}s_0))\right). \tag{1}$$

As such we can formulate the FCM of the needle as the constrained nonlinear optimization problem

$$\min_{\mathbf{r}_n} \mathcal{J}(\mathbf{r}_n) = \left\| \boldsymbol{\xi}^\mathsf{T} \left(\Phi(\mathbf{r}_n) - \mathbf{r}_s^{des} \right) \right\|_1 \tag{2}$$
$$\text{s.t.} \quad \Upsilon(\mathbf{r}_n) \leq \mathbf{0}.$$

In this equation, $\mathbf{r}_s^{\text{des}} = [\frac{\pi}{2}, 0, \frac{l_{io}}{2}, 0, \frac{\pi}{2}, 0]^\mathsf{T} \in \mathbb{R}^6$ is the desired suture parameters vector obtained from clinical criteria [23], $\mathcal{J}$ is a weighted ℓ_1 norm of suture parameter error vector, and $\boldsymbol{\xi} \in \mathbb{R}^6$ is the optimization coefficient vector that weights the importance of each suture parameter. $\Upsilon : \mathbb{R}^4 \to \mathbb{R}^7$ is a nonlinear function of suture parameters that specifies seven constraints for this problem (details provided in [27]). These constraints are to define a feasible solution set where the kinematics relationships between the needle and tissue are physically viable. For instance, Fig. 3 shows such example where the needle can be grasped by
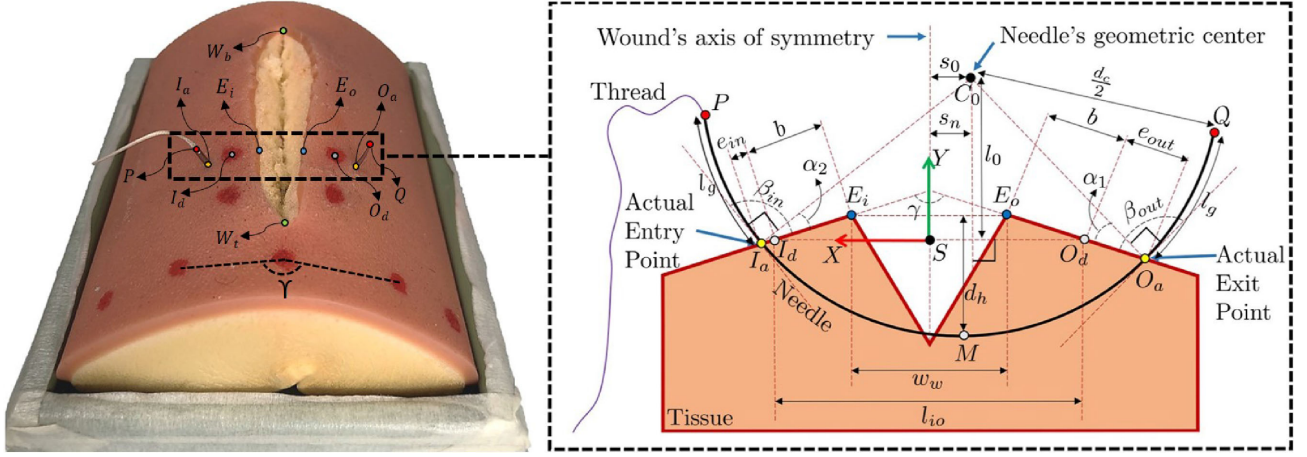
Fig. 3. Geometry of tissue phantom and parameters for stitch planning optimization.

the instruments on both sides. Υ can be formulated as follows:

$$\Upsilon(\mathbf{r}_n) = \begin{bmatrix} h_{ti} - \overrightarrow{Q}_y + b\sin(\frac{\pi-\gamma}{2}) \\ l_{\text{ins}} - l_g \\ w_w - \left|\overrightarrow{I_a O_a}\right| \\ \overrightarrow{GM}_y - b\sin(\frac{\pi-\gamma}{2}) \\ \frac{\overrightarrow{I_d I_a} \cdot \overrightarrow{I_d E_i}}{b^2} - 1 \\ \frac{\overrightarrow{O_d O_a} \cdot \overrightarrow{O_d E_o}}{b^2} - 1 \\ h_{ti} - \overrightarrow{P}_y + b\sin(\frac{\pi-\gamma}{2}) \end{bmatrix} \leq \mathbf{0}_{7\times1} \quad (3)$$

where

$$\overrightarrow{Q}_y = \begin{bmatrix} \sin(2\pi a_n) & \cos(2\pi a_n) \end{bmatrix} \overrightarrow{C_0 I_a} + l_0$$

$$\overrightarrow{C_0 I_a} = \begin{bmatrix} \frac{w_w}{2} + (b - e_{\text{in}})\cos(\frac{\pi-\gamma}{2}) - s_0 \\ e_{\text{in}}\sin(\frac{\pi-\gamma}{2}) - l_0 \end{bmatrix}$$

$$l_g = \frac{\pi a_n d_c - \frac{d_c}{2}(\gamma - \alpha_1 - \alpha_2)}{2}$$

$$|\overrightarrow{I_a O_a}| = d_c \sin(\frac{\gamma - \alpha_1 - \alpha_2}{2}).$$

In (3), $\overrightarrow{P}_y$ can be obtained analogously to $\overrightarrow{Q}_y$. This constrained optimization problem was solved using a numerical brute force algorithm. The inputs are $\boldsymbol{\xi}$, γ, l_{io}, w_w, and l_{ins} and the output is the optimal needle parameters vector that uniquely specifies the stitching path under FCM.

C. Robot Controller

This section explains the 6-DoF robot controller architecture that enables a cable-driven surgical robot to accurately follow the desired needle path, despite its inherit position inaccuracy. To this end, the camera information is incorporated into the estimation via a registration algorithm and then is used to close the differential kinematics robot controller loop.

1) Registration: To integrate the state estimation from the camera into the robot controller, the following transformation matrices must be known: $^{\text{C}}\mathbf{T}_{\text{S}}, ^{\text{C}}\mathbf{T}_{\text{B}}, ^{\text{B}}\mathbf{T}_{\text{E}}, ^{\text{E}}\mathbf{T}_{\text{Gr}}$, and $^{\text{Gr}}\mathbf{T}_{\text{NC}}$. $^{\text{C}}\mathbf{T}_{\text{S}}, ^{\text{B}}\mathbf{T}_{\text{E}}$, and $^{\text{E}}\mathbf{T}_{\text{Gr}}$ are obtained with computer vision, kinematics, and known geometric relationships, respectively. The other transformation matrices ($^{\text{C}}\mathbf{T}_{\text{B}}, ^{\text{Gr}}\mathbf{T}_{\text{NC}}$), however, are unknown, and estimated with the registration algorithms.

Registration of Robot Base to Camera: $^{\text{C}}\mathbf{T}_{\text{B}}$ defines the relationship between the robot base and the camera frames. This information is unknown as the camera is installed independently from the robot, but it can be calculated as follows:

$$^{\text{C}}\mathbf{T}_{\text{B}}{}^{\text{B}}\mathbf{T}_{\text{E}} = {}^{\text{C}}\mathbf{T}_{\text{Gr}}\left({}^{\text{E}}\mathbf{T}_{\text{Gr}}\right)^{-1} = {}^{\text{C}}\mathbf{T}_{\text{E}} \quad (4)$$

The grasper frame as measured by the camera ($^{\text{C}}\mathbf{T}_{\text{Gr}}$), along with the known transformation ($^{\text{E}}\mathbf{T}_{\text{Gr}}$), is used to obtain the robot end-effector frame in the camera frame ($^{\text{C}}\mathbf{T}_{\text{E}}$). Robot kinematics are used to calculate $^{\text{B}}\mathbf{T}_{\text{E}}$.

The problem is solved as follows. We define a function $\Theta :$ SE(3) $\rightarrow \mathbb{R}^{12}$ that maps a transformation matrix into a vector consisting of its origin and three points placed at a unit distance from the origin along the directions of each axis

$$\mathcal{S}\left(\mathbf{p} \otimes \mathbf{1}_{1\times4} + \mathbf{R}\begin{bmatrix} \mathbf{0}_{3\times1} & \mathbf{I}_3 \end{bmatrix}\right) = \Theta\left(\begin{bmatrix} \mathbf{R} & \mathbf{p} \\ \mathbf{0}_{1\times3} & 1 \end{bmatrix}\right) \quad (5)$$

where $\mathcal{S}$ is the stack operator that maps a $p \times q$ matrix into a $pq \times 1$ vector columnwise, i.e., $\mathcal{S} : \mathbb{R}^{p\times q} \rightarrow \mathbb{R}^{pq\times1}$.

The result of applying Θ to the ith sample of the measurement of $^{\text{C}}\mathbf{T}_{\text{E}}$ and $^{\text{B}}\mathbf{T}_{\text{E}}$ can be expressed as

$$\boldsymbol{\eta}_i = [\boldsymbol{\eta}_{i,o}^{\mathsf{T}} \quad \boldsymbol{\eta}_{i,x}^{\mathsf{T}} \quad \boldsymbol{\eta}_{i,y}^{\mathsf{T}} \quad \boldsymbol{\eta}_{i,z}^{\mathsf{T}}]^{\mathsf{T}} = \Theta\left({}^{\text{B}}\mathbf{T}_{\text{E}}^i\right)$$
$$\boldsymbol{\rho}_i = [\boldsymbol{\rho}_{i,o}^{\mathsf{T}} \quad \boldsymbol{\rho}_{i,x}^{\mathsf{T}} \quad \boldsymbol{\rho}_{i,y}^{\mathsf{T}} \quad \boldsymbol{\rho}_{i,z}^{\mathsf{T}}]^{\mathsf{T}} = \Theta\left({}^{\text{C}}\mathbf{T}_{\text{E}}^i\right) \quad (6)$$

In (6), $\boldsymbol{\eta}_{i,o}$ is the 3-D position of the origin of the frame $^{\text{B}}\mathbf{T}_{\text{E}}^i$. $\boldsymbol{\eta}_{i,x}$ is the 3-D position of the point with unit distance from the origin of the frame $^{\text{B}}\mathbf{T}_{\text{E}}^i$ in the x-direction of this frame. Similarly, $\boldsymbol{\eta}_{i,y}$ and $\boldsymbol{\eta}_{i,z}$ are the 3-D positions of the points with unit distance from the origin in the y and z directions, respectively. Elements of $\boldsymbol{\rho}_i$ are defined in the same manner but for the $^{\text{C}}\mathbf{T}_{\text{E}}^i$ frame. Moreover, $\boldsymbol{\eta}_i$ and $\boldsymbol{\rho}_i$ are $\in \mathbb{R}^{12}$.
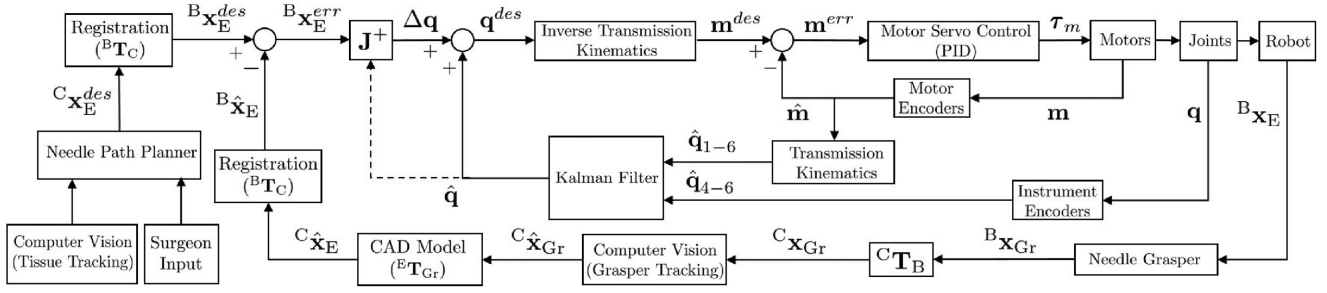
Fig. 4.   Vision-based controller for the cable-driven surgical robot (Raven IV).

For robustness of the registration, ten sets of samples are collected. The registration problem to find $^{C}\mathbf{T}_{B}$ can then be reformulated as follows:

$$\min_{\mathbf{R},\mathbf{p}} \sum_{i=1}^{m} \left\| (\mathbf{R} \otimes \mathbf{I}_4)\, \boldsymbol{\eta}_i + (\mathbf{I}_3 \otimes \mathbf{1}_{4\times 1})\, \mathbf{p} - \boldsymbol{\rho}_i \right\|_2 \tag{7}$$

$$\text{s.t.} \quad \mathbf{R}\mathbf{R}^\mathsf{T} = \mathbf{I}_3$$

where m is the number of samples (10 in this article). We solve the optimization problem in (7) (point cloud registration where correspondence between points is known) using the method suggested in [31].

Registration of Needle Center to Grasper. $^{Gr}\mathbf{T}_{NC}$ relates the needle center frame to the robot grasper frame. This registration is necessary because each time the robot grasps the needle, the grasping point on the needle is different and $^{Gr}\mathbf{T}_{NC}$ changes accordingly. To solve this problem, the needle tip is colored yellow and its position is calculated with computer vision. $^{Gr}\mathbf{T}_{NC}$ can be calculated with the following:

$$^{C}\mathbf{T}_{Gr}{}^{Gr}\mathbf{T}_{NC} = {}^{C}\mathbf{T}_{NC} \tag{8}$$

Using needle tip, needle geometry, computer-aided design (CAD) model of the grasper, and measured grasper frame, $^{C}\mathbf{T}_{NC}$ is fully defined as follows:

$$^{C}\mathbf{T}_{NC} = \begin{bmatrix} ^{C}\mathbf{r}_{NC}^{x} & ^{C}\mathbf{r}_{NC}^{y} & ^{C}\mathbf{r}_{NC}^{z} & ^{C}\mathbf{p}_{NC} \\ 0 & 0 & 0 & 1 \end{bmatrix} \tag{9}$$

where $^{C}\mathbf{r}_{NC}^{x}$, $^{C}\mathbf{r}_{NC}^{y}$, and $^{C}\mathbf{r}_{NC}^{z}$ refer to the x, y, and z vector components of the rotation matrix and $^{C}\mathbf{p}_{NC}$ is the position vector, defining the needle center frame in the camera frame. Each of these components is obtained using the following equations:

$$\begin{bmatrix} ^{C}\mathbf{p}_{NC} \\ 1 \end{bmatrix} = {}^{C}\mathbf{T}_{Gr} \begin{bmatrix} ^{Gr}\mathbf{p}_{NC} \\ 1 \end{bmatrix}$$

$$^{Gr}\mathbf{p}_{NC} = \begin{bmatrix} d_x \\ 0 \\ -d_z \end{bmatrix} \tag{10a}$$

$$^{C}\mathbf{r}_{NC}^{x} = \frac{^{C}\mathbf{p}_{NT} - {}^{C}\mathbf{p}_{NC}}{\left\| ^{C}\mathbf{p}_{NT} - {}^{C}\mathbf{p}_{NC} \right\|_2} \tag{10b}$$

$$^{C}\mathbf{r}_{NC}^{z} = {}^{C}\mathbf{r}_{Gr}^{z} \tag{10c}$$

$$^{C}\mathbf{r}_{NC}^{y} = {}^{C}\mathbf{r}_{NC}^{z} \times {}^{C}\mathbf{r}_{NC}^{x}. \tag{10d}$$

In (10a), d_x, and d_z are the position offsets (in the x and z directions, respectively) between the needle center frame and the grasper frame (see Fig. 5). These offsets are obtained using the grasper's CAD model. In (10b), $^{C}\mathbf{p}_{NT}$ is the measurement of the needle tip using the computer vision. Equation (10c) states that the z coordinates of the needle center frame and the grasper frame are identical.

Once $^{C}\mathbf{T}_{NC}$ is fully obtained as explained above, $^{Gr}\mathbf{T}_{NC}$ is then acquired using (8) with the same steps described to obtain $^{C}\mathbf{T}_{B}$.

2) Controller: The robot controller is implemented with real-time state estimation using encoders and stereo vision feedback, the registered frames, and the robot differential kinematics. The robot pose vector is defined as $\mathbf{x} \in \mathbb{R}^6$ and consists of 3-D position and orientation expressed in roll–pitch–yaw angles. The desired pose of the end-effector in the base frame is calculated from the desired path of the needle in the stitch frame using $^{B}\mathbf{T}_{E} = {}^{B}\mathbf{T}_{C}{}^{C}\mathbf{T}_{S}{}^{S}\mathbf{T}_{NC}{}^{NC}\mathbf{T}_{E}$. The error pose vector is acquired by subtracting the estimated pose from the desired

$$^{B}\mathbf{x}_{E}^{err} = {}^{B}\mathbf{x}_{E}^{des} - {}^{B}\hat{\mathbf{x}}_{E}. \tag{11}$$

The robot differential kinematics ($\mathbf{J}$) relates the joint velocities to the end-effector velocities as

$$\frac{\partial \mathbf{x}}{\partial t} = \mathbf{J}(\hat{\mathbf{q}}) \frac{\partial \mathbf{q}}{\partial t}. \tag{12}$$

The optimal displacements of the joints are then calculated from the following least squares optimization:

$$\arg\min_{\Delta \mathbf{q}} \left\| \mathbf{J}(\hat{\mathbf{q}})\Delta \mathbf{q} - {}^{B}\mathbf{x}_{E}^{err} \right\|_2. \tag{13}$$

As a result, the desired joint values are obtained with $\Delta \mathbf{q}^* \in \mathbb{R}^6$ and sent to the Raven IV through a local network. Proportional derivative (PD) joint controllers are used to internally close the loop at 1 kHz. The controller architecture is shown in Fig. 4.

For obtaining $\hat{\mathbf{q}}$, two joint angle measurements are used: one from motor encoders at 1 kHz (high frequency and low accuracy) and the other from additional encoders installed on the instruments at 250 Hz (low frequency and high accuracy). The former estimates the joint angles via transmission kinematics, which includes the pulley and gear ratios, and cable couplings while the latter (see Section II-D.2) measures the wrist joint angles only. This information is fused via a Kalman filter to estimate joint angles at 1 kHz (high frequency and high accuracy).
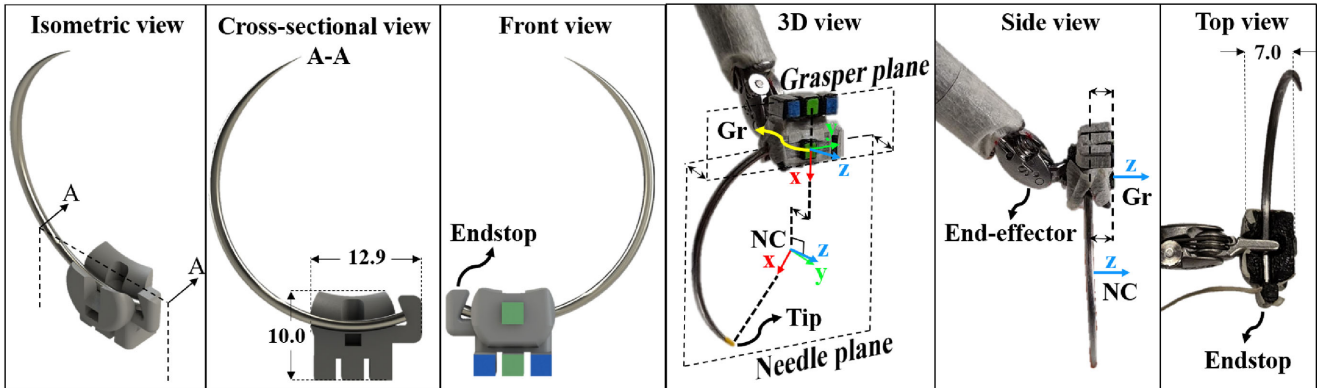
Fig. 5. Grasper design along with *NC* and *Gr* frames. All measurements are in mm.

D. Hardware Enhancements

1) Needle Grasper: In order to improve needle grasp (e.g., no needle slip) and enable accurate needle pose estimation both inside and outside the tissue, a customized color-coded 3D-printed needle grasper was designed and used (see Fig. 5). The grasper is attached to the end-effector of a large needle driver (Intuitive Surgical, Inc., Sunnyvale, CA, USA) prior to the suturing operation and permits secure grasp and release of a CTX suturing needle (Ethicon, Inc., Somerville, NJ, USA). Imperfect manual installation of the grasper may introduce small errors in $^{E}\mathbf{T}_{Gr}$ obtained from the CAD model. Since $^{E}\mathbf{T}_{Gr}$ is included in both the needle path planner and the estimator and the vision feedback is used in the controller, it is expected that such small errors do not affect the overall performance of the controller. In fact, we show that the proposed controller can successfully regulate the needle center.

To establish the kinematic relation between the needle grasper and suturing needle, the grasper holds the needle in a circular slot with curvature and width matched to those of the CTX needle. The grasper is designed such that when the large needle driver closes, the needle will enter the slot even with misalignment. As such, the center and plane of the circle created by the slot closely match those of the circle made by the needle. Additionally, to further prevent slip of the needle during suturing, an endstop is built into one side of the grasper on the inserting arm. It should be noted that the use of similar graspers for autonomous suturing has been explored by other studies, such as [18] and [32]. However, an important distinction of our design is the additional endstop that mechanically blocks the motion of the needle during the insertion phase. The needle grasper has dimensions of $9.9 \times 10.0 \times 7.0$ mm^3 for the extracting arm (without endstop) and $12.9 \times 10.0 \times 7.0$ mm^3 for the inserting arm (with endstop).

Four distinctively colored (two green, two blue) 4-mm^2 square markers are attached to the grasper at known locations, as shown in Fig. 5. These markers are detected via a vision algorithm and used to identify pose of the needle grasper. Once the needle is in contact with the endstop, it is reasonable to assume that no slip occurs. Hence, the kinematic relation between the needle center and grasper is fixed during suturing. This enables calculation of the needle center pose using the configuration of the needle grasper, even when the needle is obscured.
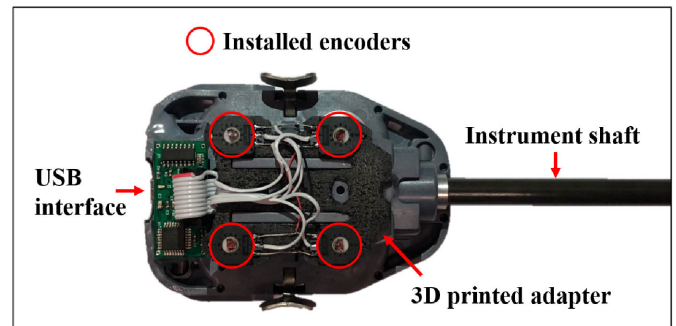

Fig. 6. Additional encoders installed on the surgical instrument.

2) Enhanced Instrument With Additional Encoders: As the wrist joints of surgical instruments are the farthest operation points from the robot base, they have higher kinematic inaccuracy in a cable-driven surgical robot. To reduce this error, we mounted four additional low-cost encoders and a custom-made microcontroller board in a 3-D printed adaptor on the spindle side of the da Vinci instruments (see Fig. 6). These resistive rotary position sensors are used to obtain kinematic knowledge of the instrument's wrist and jaws by directly measuring rotation of the spindles that drive the instrument's tip through cables in the instrument shaft. Due to the coupled motions of the wrist and jaws, as well as a possible misalignment between the spindle and the tool tip angles, an offline calibration procedure is performed. This manual calibration is done by measuring the spindle angles and the corresponding tool tip angles at various tip poses. During operation, the spindle data are converted into four absolute tool joint values of roll, pitch, yaw, and open/close of the gripper's jaw, which are sent to the control PC at 250 Hz with precision of $0.3°$.

E. Computer Vision Algorithms

For tracking the different elements of the suturing framework such as tissue and grasper, OpenCV library [33] and color segmentation filters in HSV (hue, saturation, value) space are used for image processing. More specifically, the contours of markers are obtained, and the centers of the contours are selected as the pixel positions of the markers. The corresponding markers in the

left and the right images are paired and their 2-D pixel values are used to calculate their 3-D positions using triangulation. We deployed built-in functions in OpenCV to perform these image processing operations.

1) Needle Pose Estimation: In general, two methods for estimating pose of the needle using vision have been studied in the literature. The first method is direct measurement of the suturing needle [18], [20]. The other method involves indirect estimation of the needle pose via measurement of external features and known kinematic relationship [24], [26].

Our approach consists of a combination of the two methods in order to exploit the advantages of both. Estimation of five DOFs of the needle pose is obtained by indirect measurement using the customized grasper. The last DOF, which is dependent on where the grasper holds the needle, is obtained by direct measurement of the needle tip and is used to register the needle center to the grasper. The estimation of this last DOF (the x-axis of NC shown in Fig. 5) is only performed when the robot grasps/regrasps the needle. Since the needle tip measurement is essential for estimation of needle pose, the desired grasp point on the needle for the extracting arm is selected such that the grasper does not occlude the needle tip. Of note, this is possible due to the fact that the needle tip position from vision and the needle tip orientation from the grasper are known. This hybrid estimation method provides two main advantages over the approaches in the literature. First, indirect measurements enable continuous knowledge of needle pose both inside and outside the tissue. Second, none of the previous indirect measurement methods were applied to a surgical robot with articulated wrists. Our customized grasper can be easily installed on the robot's large needle driver without any modifications.

Grasper Frame (Gr). Any point $\mathbf{u} \in \mathbb{R}^3$ on the grasper plane satisfies $\mathbf{u}^\mathsf{T}\mathbf{z} = d$ where $\mathbf{z} \in \mathbb{R}^3$ and $d \in \mathbb{R}$ are the normal vector and bias parameters of the plane. We identify the grasper plane as the one coincident to the four markers. To this end, we formulate a least squares problem as follows:

$$\arg\min_{\mathbf{z}} \|\mathcal{M}\mathbf{z} - d \times \mathbf{1}_{4\times 1}\|_2$$

$$\text{s.t. } \mathbf{z}^\mathsf{T}\begin{bmatrix} 0 \\ 0 \\ 1 \end{bmatrix} \leq 0, \|\mathbf{z}\|_2 = 1 \tag{14}$$

where $\mathcal{M} \in \mathbb{R}^{4\times 3}$ is a matrix with the 3-D positions of the markers rowwise. Of note, the inequality in (14) is to make sure that the direction of the normal vector is toward the camera. To solve this optimization problem, solvers such as [34] could be used. However, for simplicity, we use an approximate solution by first solving an unconstrained problem and then projecting the solution on to the constraint set. To do so, we first set $d = 1$ and solve the linear least square $\mathcal{M}\hat{\mathbf{z}} = \mathbf{1}_{4\times 1}$ that has the solution of $\hat{\mathbf{z}} = (\mathcal{M}^\mathsf{T}\mathcal{M})^{-1}\mathcal{M}^\mathsf{T}\mathbf{1}_{4\times 1}$. Once we get $\hat{\mathbf{z}}$, the solutions for $\mathbf{z}$ and d of the original problem are $\hat{\mathbf{z}}/\|\hat{\mathbf{z}}\|_2$ and $1/\|\hat{\mathbf{z}}\|_2$, respectively. If the third element of $\mathbf{z}$ is positive (i.e., the normal vector is not pointing toward the camera), we negate both $\mathbf{z}$ and d. A ten-sample moving average filter was used to reduce the noise. The x-coordinate of the grasper frame (Gr) lies along the vector

passing through the green markers. The origin of Gr is located on one of the green markers as shown in Fig. 5. The grasper plane and frame are depicted in Fig. 5.

Needle Center Frame (NC). As depicted in Fig. 5, the needle plane is defined as the plane passing through the NC parallel to the grasper plane. The needle center position is obtained from the measured Gr and the grasper CAD model. The z-coordinate of NC is set to be parallel to that of Gr. The x-coordinate is the vector from the needle center position to the needle tip position. A Kalman filter is exploited to smooth the positions of the needle center and grasper origins as follows:

$$\boldsymbol{\nu}_{k+1} = \begin{bmatrix} \mathbf{I}_3 & \Delta t \times \mathbf{I}_3 & \mathbf{0}_{3\times 3} & \mathbf{0}_{3\times 3} \\ \mathbf{0}_{3\times 3} & \mathbf{I}_3 & \mathbf{0}_{3\times 3} & \mathbf{0}_{3\times 3} \\ \mathbf{0}_{3\times 3} & \mathbf{0}_{3\times 3} & \mathbf{I}_3 & \Delta t \times \mathbf{I}_3 \\ \mathbf{0}_{3\times 3} & \mathbf{0}_{3\times 3} & \mathbf{0}_{3\times 3} & \mathbf{I}_3 \end{bmatrix} \boldsymbol{\nu}_k + \mathbf{w}_k$$

$$\mathbf{y}_k = \begin{bmatrix} \mathbf{I}_3 & \mathbf{0}_{3\times 3} & \mathbf{0}_{3\times 6} \\ \mathbf{0}_{3\times 6} & \mathbf{I}_3 & \mathbf{0}_{3\times 3} \end{bmatrix} \boldsymbol{\nu}_k + \mathbf{v}_k \tag{15}$$

where k is the time instance, $\boldsymbol{\nu} \in \mathbb{R}^{12}$ is a state vector consisting of positions and velocities of the needle center and grasper origins, and $\mathbf{y} \in \mathbb{R}^6$ is a measurement vector of the positions of the origins. Moreover, the process noise $\mathbf{w}$ and measurement noise $\mathbf{v}$ are random vectors assumed to be uncorrelated, zero-mean with normal probability distributions. Of note, the use of this Kalman filter enables a continuous estimation of the needle position even when the markers are occluded.

2) Tissue Tracking Algorithm: The needle path planning algorithm requires the wound width (w_w), tissue angle (γ), desired needle entry point (I_d), and desired needle exit point (O_d) from the vision system. For estimating γ, five distinctive red dots were placed on the edge of the tissue closest to the camera. Two pairs of red dots were placed across the wound, with each pair representing I_d and O_d. For obtaining w_w, which is the Euclidean distance between E_o and E_i, the tissue wound was tracked using the standard OpenCV contour detection. The wound edges (E_o and E_i) were selected as the wound contour points with minimum Euclidean distance to the I_dO_d line.

Stitch Frame (S). The origin of S (see Fig. 3) is the midpoint of the I_dO_d line. The x-coordinate and z-coordinate are defined by unit vectors of $\overrightarrow{O_dI_d}$ and $\overrightarrow{W_tW_b}$, respectively.

III. EXPERIMENT

To evaluate the efficacy of the autonomous suturing framework, first we assessed the needle pose estimation algorithm. Second, we performed autonomous suturing experiments based on a finite-state machine (FSM) illustrated in Fig. 7. We refer to the first as *needle pose evaluation (NPE)* and the second as *autonomous suturing evaluation (ASE)*. Experiments were performed using the cable-driven Raven IV surgical robotic system along with a stereo vision system and tissue phantoms. Experiments were designed so that they cover a wide variety of real surgical scenarios and surgeon inputs. We assessed the performance of the system based on needle estimation accuracy,
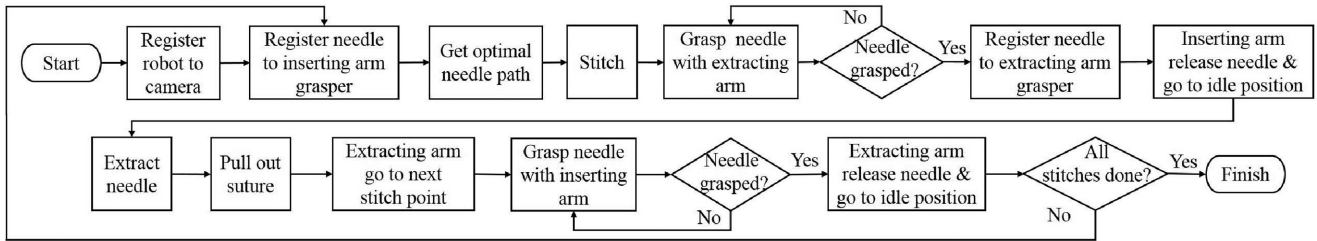
Fig. 7. Finite state machine for autonomous bimanual suturing.

suture parameters, and accuracy of the performed stitching trajectories.

A. Experiment Setup

1) Robotic System: We used the Raven IV (see Fig. 1), an open-platform cable-driven surgical robot [4] with four robotic manipulators. Each manipulator consists of a 3-DoF spherical positioning mechanism outfitted with an additional 4-DoF large needle driver.

2) Stereo Vision System: To realize the proposed estimation and control architecture, a stereo camera (Blackfly-BFLY-U3-13S2C, Point Grey Research, Inc., Richmond, BC, Canada) is deployed. The frame rate of the stereo camera is 30 Hz with downsampled image resolution of 644×482 pixels.

3) Tissue Phantom: To assess performance in various environments, two tissue phantoms from Simulab Corporation, Seattle, WA, USA, were used: a Tissue Suturing Model (TSM-10) and an Injectable Tissue Model (ITM-30). To quantify mechanical properties, force–displacement response of each was measured by puncturing a needle into the skin and fat using 5960 dual column table top testing system (Instron, Inc., Norwood, MA, USA). The stiffness range of the skin and subcutaneous fat of TSM-10 are 0.01 (N/mm) to 0.03 (N/mm) and 0.014 (N/mm) to 0.015 (N/mm), respectively. The stiffness range of the skin and subcutaneous fat of ITM-30 are 0.12 (N/mm) to 0.21 (N/mm) and 0.05 (N/mm) to 0.08 (N/mm), respectively. Based on this data, we refer to TSM-10 as *soft tissue* and ITM-30 as *hard tissue*. A Contoured Tissue Tray (CTT-10) was used to immobilize each tissue phantom.

B. Experiment Design

1) Needle Pose Evaluation (NPE): Since the needle pose estimation is obtained from the needle grasper measurements and affects the overall performance of the system, it is crucial to evaluate the accuracy of our estimation algorithm. Obtaining an accurate ground truth of the needle center pose is rather abstract and challenging as it is not physically accessible and/or visible [18]. Hence, a structure for needle estimation (SNE), which encloses the needle, was designed and 3-D printed (see Fig. 8). Three red markers are placed on the SNE to uniquely define the needle pose using computer vision. It is expected that the SNE provides higher accuracy pose estimation than the needle grasper. This is because in the SNE, the marker 2 is colocated with the needle center (see Fig. 8(a)) and smaller markers
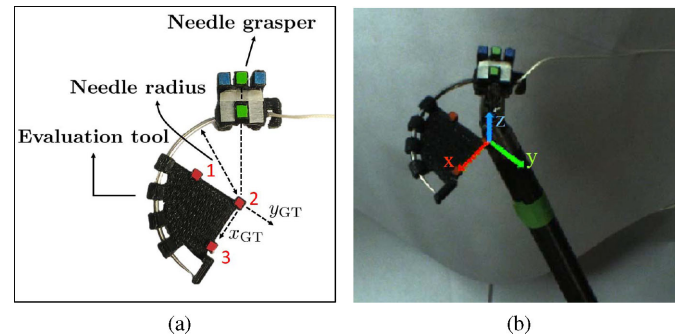

Fig. 8. Illustration of needle pose estimation evaluation results. Each figure shows (a) SNE and (b) representative configuration as well as the needle pose estimation from the needle grasper.

are used, which reduce the errors from pixel correspondence. Therefore, needle pose estimation from the SNE is used for ground truth.

This NPE method can capture errors in estimating the relationship between the needle center and the grasper pose ($^{Gr}\mathbf{T}_{NC}$). A possible source for these errors could be misalignment of the needle inside the grasper. Note that using this method, however, we cannot assess the errors from the intrinsic/extrinsic calibration of the stereo camera system as we deploy the same vision system for obtaining the ground truth. Such errors, however, were greatly reduced by proper tuning of the parameters using conventional calibration methods as in [33].

2) Autonomous Suturing Evaluation (ASE): In [27], the proposed novel needle path planning algorithm was evaluated in simulation and only a single scenario with an open-loop controller (i.e., no vision feedback) was tested in a physical environment. In order to fully verify the algorithm, we expand on the previous work by testing under multiple sets of suturing criteria within different physical environments using closed-loop vision feedback. Additionally, it is necessary to evaluate the accuracy and robustness of the proposed solutions for servoing a cable-driven surgical robotic system in autonomous suturing.

The ASE consisted of performing four sets of suturing experiments. Each set is one permutation of two different surgeon inputs (ξ) for the path planning algorithm and the two different tissue phantoms. The different surgeon inputs are chosen so that one favors a deep suture (i.e., $\|\xi\|_\infty = \xi_3$) while the other encourages entering/exiting the needle to/from the desired entry/exit points (i.e., $\|\xi\|_\infty = \xi_2 = \xi_6$). We refer to the former as *deep suture* and the later

as *point suture*. In the ASE experiments, the selected values are $\boldsymbol{\xi} = [0.025, 0.025, 0.45, 0.45, 0.025, 0.025]^\mathsf{T}$ and $\boldsymbol{\xi} = [0.033, 0.3, 0.033, 0.3, 0.033, 0.3]^\mathsf{T}$ for the deep suture and the point suture, respectively. These two surgeon inputs result in two different desired needle paths. In addition to this clinical motivation, the selection of different needle reference trajectories enables us to assess the accuracy of the proposed solutions under different robot dexterity within suturing workspace. The two significantly different tissue phantoms were chosen to test the robustness of framework across a range of tissue properties (e.g., stiffness).

To evaluate the repeatability of the system, each of the four sets of experiments consisted of four trials. For each trial, the operator (surgeon) first selects the optimization coefficients ($\boldsymbol{\xi}$) to imply preferred suture parameters. A needle path is then generated with the path planning algorithm. Finally, autonomous suturing is performed based on the FSM. One important aspect of this autonomous suturing framework is the needle grasping method. This method is such that once the robot is controlled to the desired pose to grasp the needle, the robot closes the jaws to grasp the needle while staying stationary. As mentioned earlier, the design of the grasper is such that the needle orientation would be automatically adjusted to account for needle–grasper misalignment. Such adjustment motions of the needle might introduce undesirable stress on the tissue when the extracting arm is grasping the needle. The adjustment motions, however, are small due to a good control accuracy of our framework shown in the results.

C. Performance Evaluation Metrics

1) Structure for Needle Estimation (SNE): To quantify the accuracy of the 6-DoF needle pose estimation, the needle center pose is measured with the grasper (actual) and compared against the one from SNE (ground truth). The actual pose was expressed in the ground truth frame (see Fig. 8) and error positions and Euler angles are acquired.

2) Autonomous Suturing Evaluation (ASE): Accurate motion control of the needle inside the tissue is important for a successful suturing. We evaluate the efficacy of the proposed automated suturing from two perspectives: robot control in an unknown tissue environment; and medical suturing requirements.

From the control perspective, the root-mean-square error (RMSE) of the needle trajectory during stitching and extraction is presented. From the clinical perspective, the suture parameters of the needle path planning are used to evaluate the system performance and suture quality.

IV. RESULTS

A. Needle Pose Estimation Error

The needle was placed at ten random configurations within the required workspace to evaluate the pose estimation. Fig. 8(b) depicts one such configuration. At each configuration, 500 data samples were collected at 30 Hz. The mean and standard deviation of the estimation errors are reported in Table II. As can

TABLE II
NEEDLE POSE ESTIMATION EVALUATION RESULT

DoF	x (mm)	y (mm)	z (mm)	roll (deg)	pitch (deg)	yaw (deg)
Mean	0.46	0.87	0.61	2.88	3.46	2.17
Std.	0.30	0.59	0.47	2.50	2.25	1.65

be calculated, our proposed estimation method results in RMSE of 0.67 mm in position and 2.89° in orientation.

B. Needle Trajectory Following Error

A total of 16 (2 tissue phantoms $\times$ 2 reference needle trajectories $\times$ 4 repetitions) trials were performed for ASE. Six snapshots of automated suturing for each permutation of tissue phantom and reference needle trajectory are illustrated in Fig. 9. A sample of 2-D and 3-D needle tip and center trajectories are shown in Fig. 10 and the RMSE of the needle center tracking is summarized in Table III. Regarding the orientation and its error, the main component that matters is the orientation of the needle plane (which is determined by its normal vector) compared to the desired plane of the needle. This is because, if this needle plane as well as the needle center are well regulated, it is expected that the needle tip follows desired trajectory under FCM. To this end, the RMSE of the orientation is obtained by the error between the desired and actual normal vectors of the needle plane along the suturing trajectory. As can be seen, using our proposed framework for automated suturing resulted in a successful regulation of the needle center to the desired fixed point (from the optimization). The position and orientation RMSE of this regulation are less than 2.37 mm and 4.71° for each trial and averaged 2.07 mm and 4.29° across all trials.

C. Suture Parameters

To evaluate our algorithm based on clinical suturing criteria, the suture parameters defined in Section II-B are quantified. After each trial, 2-D and 3-D positions of the actual needle entry (I_a) and exit (O_a) points are retrieved from the images. The suture depth (d_h) was obtained using the following equation:

$$d_h = \begin{bmatrix} 0 & 1 & 0 & 0 \end{bmatrix} \left({}^\mathrm{C}\mathbf{T}_\mathrm{S} \right)^{-1} \begin{bmatrix} M - \left(\frac{E_o + E_i}{2} \right) \\ 1 \end{bmatrix} \qquad (16)$$

where M is acquired by selecting the deepest point of the needle tip trajectory with the brute-force search method. Entry (β_in) and exit (β_out) angles are obtained from (1) using the measured positions of the needle center as well as the actual entry/exit points. The suture symmetry (s_n) is calculated as follows:

$$s_n = \left| \begin{bmatrix} 1 & 0 & 0 & 0 \end{bmatrix} \left({}^\mathrm{C}\mathbf{T}_\mathrm{S} \right)^{-1} \begin{bmatrix} M \\ 1 \end{bmatrix} \right|. \qquad (17)$$

Experiment results for each trial are reported in Table IV and the mean and standard deviations are reported in Table V.

As the needle tip and center information can be continuously measured using the needle grasper, even when the needle is inside the tissue, the entry and exit angles of the needle can
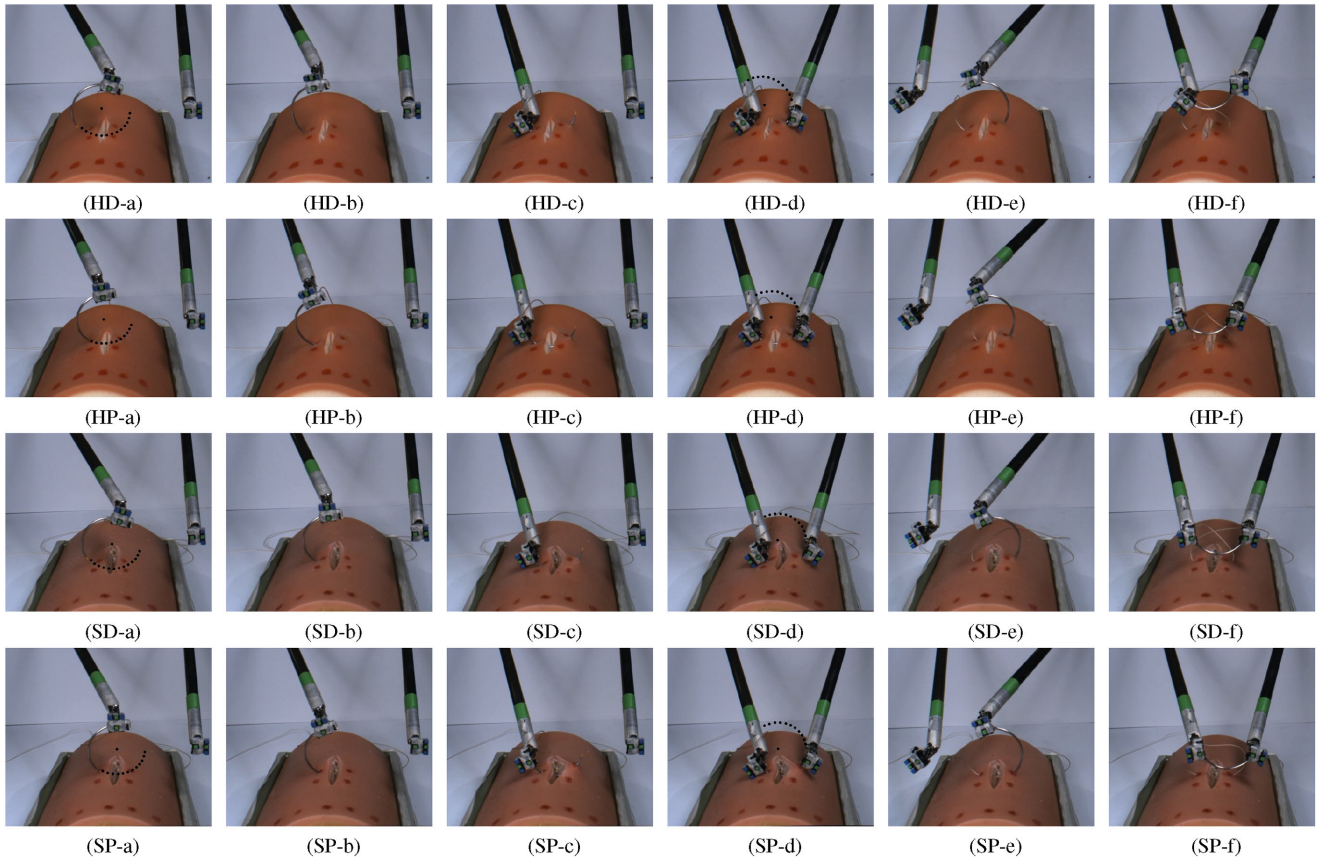
Fig. 9. Representative snapshots of experiments. S: Soft tissue. H: Hard tissue. D: Deep suture. P: Point suture. (a) Grasping the needle with the inserting arm. (b) Moving toward the wound and entering the tissue perpendicularly. (c) Stitching. (d) Approaching and grasping the needle with the extracting arm. (e) Extracting the needle. (f) Handing off to the inserting arm. The desired trajectories for the inserting arm (a) and extracting arm (d) are plotted with black dots.

TABLE III
RMSE OF NEEDLE CENTER POSE CONTROL

Experiment set	Position	Exp.1	Exp.2	Exp.3	Exp.4	Orientation	Exp.1	Exp.2	Exp.3	Exp.4
Hard Tissue Deep Suture	Mean (mm)	2.14	2.15	2.19	1.94	Mean (deg)	4.22	4.63	4.51	3.76
	Std. (mm)	1.01	0.92	0.95	0.87	Std. (deg)	3.02	2.74	2.57	2.14
Hard Tissue Point Suture	Mean (mm)	2.37	1.93	1.93	1.92	Mean (deg)	4.25	4.32	4.59	4.21
	Std. (mm)	0.98	0.71	0.87	0.75	Std. (deg)	2.48	2.72	2.31	2.50
Soft Tissue Deep Suture	Mean (mm)	2.17	2.08	2.19	2.09	Mean (deg)	4.27	4.55	4.67	4.71
	Std. (mm)	0.95	0.88	0.92	0.90	Std. (deg)	2.34	2.67	2.75	3.31
Soft Tissue Point Suture	Mean (mm)	2.01	2.03	1.91	2.06	Mean (deg)	3.42	4.31	4.15	4.05
	Std. (mm)	0.77	0.91	0.87	0.75	Std. (deg)	2.03	2.86	2.03	2.16

The position data consist of the 3-D needle center positions and the orientation data consist of the normal vector of the needle plane.

be calculated over the entire stitching. These angles are plotted in Fig. 11 for a representative trial.

V. DISCUSSION AND CONCLUSION

The needle pose estimation results include information of the compound pose error across all sources. These include errors from imperfect grasp, camera noise, pixel correspondence, 3-D printing resolution, and manual installation of markers. Despite these possible sources of errors, the needle grasper provides accurate pose information. The average and standard deviation of the position errors across the ten configurations were under 0.87 mm and 0.59 mm, respectively. Similarly, the orientation error average and standard deviation in each direction were under 3.46° and 2.50°, respectively. This indicates that the custom needle grasper both correctly grasped the needle and can be used with vision algorithms to obtain submillimeter accuracy for needle pose estimation.

The RMSE of the needle trajectory following confirms the capability of our system to maneuver the needle inside the

TABLE IV
SUTURE PARAMETERS OF ASE EXPERIMENTS

	Entry distance $e_{in}(mm)$		Entry angle $\beta_{in}(degrees)$		Suture depth $d_h(mm)$		Symmetry $s_n(mm)$		Exit distance $e_{out}(mm)$		Exit angle $\beta_{out}(degrees)$	
	Desired	Error	Desired	Error	Desired	Error	Desired	Error	Desired	Error	Desired	Error
	— Hard tissue, suture Depth prioritized (HD)											
Exp.1	4.40	0.04	128.41	10.42	6.06	1.21	0.00	0.86	4.40	0.43	128.41	0.93
Exp.2	4.48	0.95	128.41	7.45	6.03	0.10	0.00	0.54	4.48	0.18	128.41	1.84
Exp.3	4.76	0.75	128.98	0.39	5.96	0.65	0.00	0.43	4.76	0.17	128.98	2.79
Exp.4	4.91	0.04	128.98	5.80	5.93	0.22	0.00	0.36	4.91	0.34	128.98	1.77
	Hard tissue, entry/exit Points prioritized (HP)											
	Desired	Error	Desired	Error	Desired	Error	Desired	Error	Desired	Error	Desired	Error
Exp.1	0.28	1.04	137.58	1.69	3.49	0.13	0.00	0.37	0.28	2.55	137.58	6.55
Exp.2	0.33	0.65	139.30	2.42	3.32	0.86	0.00	1.40	0.33	2.31	139.30	12.75
Exp.3	0.25	1.00	137.58	4.06	3.45	0.03	0.00	0.20	0.25	2.15	137.58	6.40
Exp.4	0.09	0.57	138.73	5.54	3.35	0.70	0.00	0.27	0.09	1.84	138.73	8.02
	Soft tissue, suture Depth prioritized (SD)											
	Desired	Error	Desired	Error	Desired	Error	Desired	Error	Desired	Error	Desired	Error
Exp.1	4.14	0.98	125.54	0.41	6.18	0.60	0.00	0.63	4.14	1.30	125.54	1.16
Exp.2	4.14	0.34	123.82	0.92	6.29	1.91	0.00	0.09	4.14	0.82	123.82	1.91
Exp.3	4.26	0.43	124.39	3.18	6.22	0.28	0.00	0.00	4.26	0.70	124.39	0.44
Exp.4	4.32	0.32	126.11	2.79	6.06	1.01	0.00	0.03	4.32	0.88	126.11	0.06
	Soft tissue, entry/exit Points prioritized (SP)											
	Desired	Error	Desired	Error	Desired	Error	Desired	Error	Desired	Error	Desired	Error
Exp.1	0.50	0.50	145.61	6.89	2.11	0.14	0.00	1.09	0.50	1.41	145.61	3.33
Exp.2	0.13	1.55	139.30	4.81	3.28	0.57	0.00	0.12	0.13	0.94	139.30	2.28
Exp.3	0.00	1.30	139.87	1.28	3.22	0.11	0.00	0.49	0.00	0.86	139.87	4.21
Exp.4	0.15	0.93	135.86	1.94	3.59	0.96	0.00	0.69	0.15	0.61	135.86	1.77
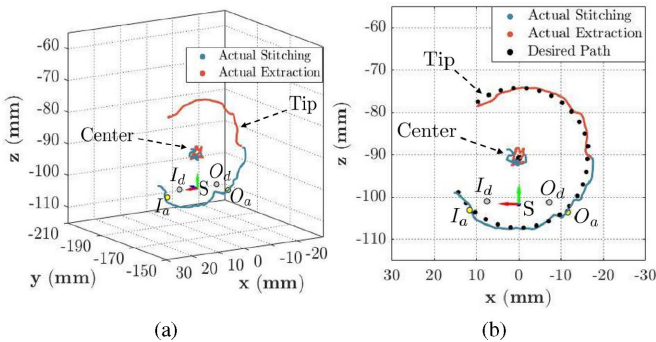
Fig. 10.   Needle tip and center trajectories in (a) 3-D and (b) 2-D.

TABLE V
STATISTICS OF SUTURE PARAMETER ERRORS IN ASE.

Exp.	Stat.	e_{in} (mm)	β_{in} (deg)	d_h (mm)	s_n (mm)	e_{out} (mm)	β_{out} (deg)
HD	Mean	0.45	6.02	0.55	0.55	0.28	1.83
	Std.	0.47	4.21	0.50	0.22	0.13	0.76
HP	Mean	0.81	3.43	0.43	0.56	2.21	8.43
	Std.	0.24	1.72	0.41	0.56	0.30	2.97
SD	Mean	0.52	1.82	0.95	0.19	0.93	0.89
	Std.	0.31	1.36	0.71	0.30	0.26	0.82
SP	Mean	1.07	3.73	0.44	0.60	0.95	2.90
	Std.	0.46	2.61	0.40	0.40	0.33	1.09

tissue phantoms. The needle center position was regulated to a stationary reference point as the needle was rotating inside the tissue. The RMSEs are shown to be consistent with maximum and average of 2.37 mm and 2.07 mm for position and 4.71° and 4.29° for orientation across all trials. This result, which was obtained in complex tissue environments, is a drastic improvement over the Raven IV internal kinematics controller with 26-mm position and 20.6° orientation regulation error in an obstacle-free environment [35]. Based on these results, it is concluded that the proposed enhanced hardware and

software solutions achieved excellent performance in environments with different properties. Moreover, this also confirms that the proposed scheme performed well across both reference needle trajectories requiring dissimilar robot dexterity.

The proposed automated suturing framework resulted in a close match between the desired and actual suturing parameters. The averaged errors across all experiments were 0.71 mm and 1.09 mm for the entry and exit points, 3.75° and 3.51° for the entry and exit angles, and 0.48 mm and 0.59 mm for the suture symmetry and depth. As the needle path planning algorithm is
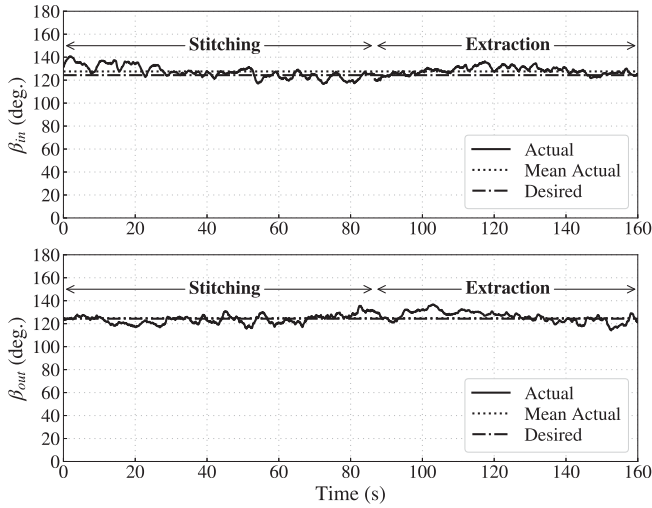
Fig. 11.   Desired and actual entry and exit angles of the needle in a representative experiment of ASE.

of the needle center (l_o, s_o), which is calculated as follows:

$$\frac{\partial \beta_{\text{in}}}{\partial l_0} = \frac{2\sin(\frac{\gamma}{2})}{d_c \left|\cos(\alpha_2)\right|}, \frac{\partial \beta_{\text{in}}}{\partial s_0} = \frac{\partial \beta_{\text{in}}}{\partial l_0}\tan(\frac{\pi - \gamma}{2}). \quad (18)$$

These SVs essentially specify the errors in entry angle (β_{in}) per unit needle displacements in x and y directions of the tissue frame. For our experiments, these SVs are calculated as 3.96 (°/mm) and 0.75 (°/mm) in y and x directions, respectively. This result shows that needle center positioning error along the vertical direction of the stitch frame is more significant and results in $\sim 6\times$ errors in entry angles than that in the horizontal direction. Similar result can be derived for β_{out}. Moreover, this sensitivity analysis can explain the actual entry/exit angles reported in Fig. 11. From the experiment results (see Fig 10(b)), it was found that error ranges for the needle center positioning are 4.42 mm and 4.09 mm in x and y directions, respectively. Based on these errors and calculated SVs, the expected error ranges from the sensitivity analysis for entry and exit angles are 16.53°, which are similar to data reported in Fig. 11.

While the proposed software and hardware solution enabled autonomous suturing, there are some limitations that should be addressed in the future work. First, the framework is developed to automate steps (II)–(V) and (VII) of a full suturing task. To automate the remaining steps (I) and (VI), an identical vision-based controller could be used while new motion planning and estimation algorithms must be developed. Studies such as in [36]–[38] are some examples of such algorithms. Second, the robustness of the color segmentation algorithms to environmental changes could be improved using more advanced algorithms, such as convolutional neural networks. Third, enhanced 3-D tissue reconstruction algorithms could be used for a more complicated surgical environment involving various tissue types and blood. Fourth, one of the important factors contributing to slow robot motion is the frequency of the estimation algorithm. This can be improved by deploying a stereo camera system with a higher update rate, which would increase the estimation and control sampling rates. Finally, the proposed framework could be expanded by including active tissue manipulation into the algorithm. For example, if the tissue configuration is not proper for suturing (i.e., the wound is too wide), the extracting arm could manipulate the tissue and change its configuration such that the inserting arm could perform stitching.

In this article, we propose a novel estimation, control and planning framework for the robotic automation of surgical suturing. The framework combines a kinematic-based needle path planner, a grasper-based needle pose estimator, and an accurate 6-DoF controller of a cable-driven surgical robotic system. The results confirmed a submillimeter position estimation accuracy of the needle pose and indicated that our framework improves the internal robot kinematic controller by at least factors of 10 and 5 in position and orientation, respectively. The autonomous suturing experiments confirmed that the robot is able to accurately follow the reference needle trajectories and deliver the desired suture parameters suggested by the planner. Additionally, our experiment results showed a robust performance of the autonomous suturing framework across various environments with

designed to minimize tissue trauma, these small errors demonstrate the efficacy of the proposed approach from a clinical perspective. This close match further validates the accuracy of the needle controller.

In comparison to our prior study [27], which primarily confirmed the effectiveness of the novel needle path planner within a simulation environment, the results of the 16 trials in this article confirm it experimentally. This is evaluated in terms of the generated path and the success of the suture. First, as reported in Table IV, the generated path provides reasonable sutures while correctly prioritizing suture parameters corresponding to higher selected (ξ). This is demonstrated by suture depth closely matching the surgeon desired value at the expense of entry/exit angles in deep suture experiments (HD/SD). Similarly, the entry/exit points closely match the surgeon desired values at the expense of suture depth in point suture experiments (HP/SP). Second, all of the optimized paths resulted in kinematically valid trajectories. The constraints embedded in the optimization algorithm correctly prevented undesirable scenarios, such as contact between the robot arm and tissue throughout stitching and extraction.

While the errors between actual and desired suture parameters are small, it is observed that the exit distance and angle errors of HP experiments are comparably larger (see Table V). This may be explainable by the needle deviation from the reference trajectory that occurs when the needle pierces the skin layer of the hard tissue as suggested by Nageotte *et al.* [21]. Since the suture path is shorter for HP compared to HD and tissue phantom is stiffer for HP compared to SP, it is more difficult for the controller to compensate this deviation, resulting in the larger error in exit distance and angles. However, even with the nonhomogenous hard tissue phantoms, these errors are < 2.55 mm and $< 12.75°$ for exit point and angle, respectively.

The errors in β_{in} (β_{out}) across trials can be analyzed with the sensitivity value (SV) of the β_{in} (β_{out}) with respect to position

different mechanical properties as well as dissimilar trajectories requiring different robot dexterity.

REFERENCES

[1] M. Yip and N. Das, "Robot autonomy for surgery," in *Encyclopedia of Medical Robotics*, ch. 10, Singapore: World Scientific, 2017, pp. 281–313.

[2] G.-Z. Yang *et al.*, "Medical robotics—Regulatory, ethical, and legal considerations for increasing levels of autonomy," *Sci. Robot*, vol. 2, no. 4, 2017, Art. no. eaam8638.

[3] G. S. Guthart and J. K. Salisbury, "The Intuitive/sup TM/telesurgery system: Overview and application," in *Proc. Millennium Conf. IEEE Int. Conf. Robot. Autom. Symp.*, 2000, vol. 1, pp. 618–621.

[4] B. Hannaford *et al.*, "Raven-II: An open platform for surgical robotics research," *IEEE Trans. Biomed. Eng.*, vol. 60, no. 4, pp. 954–959, Apr. 2013.

[5] M. Haghighipanah, Y. Li, M. Miyasaka, and B. Hannaford, "Improving position precision of a servo-controlled elastic cable driven surgical robot using unscented Kalman filter," in *Proc. IEEE/RSJ Int. Conf. Intell. Robots Syst.*, 2015, pp. 2030–2036.

[6] A. Kapoor, M. Li, and R. H. Taylor, "Spatial motion constraints for robot assisted suturing using virtual fixtures," in *Proc. Int. Conf. Med. Image Comput. Comput.-Assisted Intervention*, 2005, pp. 89–96.

[7] A. Abiri *et al.*, "Suture breakage warning system for robotic surgery," *IEEE Trans. Biomed. Eng.*, vol. 66, no. 4, pp. 1165–1171, Apr. 2019.

[8] J. Ruurda, I. Broeders, B. Pulles, F. Kappelhof, and C. Van der Werken, "Manual robot assisted endoscopic suturing: Time-action analysis in an experimental model," *Surg. Endoscopy Interventional Techn.*, vol. 18, no. 8, pp. 1249–1252, 2004.

[9] C. Shin, P. W. Ferguson, S. A. Pedram, J. Ma, E. P. Dutson, and J. Rosen, "Autonomous tissue manipulation via surgical robot using learning based model predictive control," in *Proc. IEEE Int. Conf. Robot. Autom.*, 2019, pp. 3875–3881.

[10] F. Alambeigi, Z. Wang, R. Hegeman, Y.-H. Liu, and M. Armand, "A robust data-driven approach for online learning and manipulation of unmodeled 3-d heterogeneous compliant objects," *IEEE Robot. Autom. Lett.*, vol. 3, no. 4, pp. 4140–4147, Oct. 2018.

[11] F. Alambeigi, Z. Wang, Y.-H. Liu, R. H. Taylor, and M. Armand, "Toward semi-autonomous cryoablation of kidney tumors via model-independent deformable tissue manipulation technique," *Ann. Biomed. Eng.*, vol. 46, no. 10, pp. 1650–1662, 2018.

[12] S. A. Pedram *et al.*, "Toward synergic learning for autonomous manipulation of deformable tissues via surgical robots: An approximate Q-learning approach," in *Proc. 8th IEEE RAS/EMBS Int. Conf. Biomed. Robot. Biomechatronics*, 2020.

[13] A. Murali *et al.*, "Learning by observation for surgical subtasks: Multilateral cutting of 3d viscoelastic and 2d orthotropic tissue phantoms," in *Proc. IEEE Int. Conf. Robot. Autom.*, 2015, pp. 1202–1209.

[14] A. Garg *et al.*, "Tumor localization using automated palpation with Gaussian process adaptive sampling," in *Proc. IEEE Int. Conf. Autom. Sci. Eng.*, 2016, pp. 194–200.

[15] T. Liu and M. C. Cavusoglu, "Needle grasp and entry port selection for automatic execution of suturing tasks in robotic minimally invasive surgery," *IEEE Trans. Autom. Sci. Eng.*, vol. 13, no. 2, pp. 552–563, Apr. 2016.

[16] A. Shademan, R. S. Decker, J. D. Opfermann, S. Leonard, A. Krieger, and P. C. Kim, "Supervised autonomous robotic soft tissue surgery," *Sci. Transl. Med.*, vol. 8, no. 337, pp. 337–346, 2016.

[17] H. Dehghani, S. Farritor, D. Oleynikov, and B. Terry, "Automation of suturing path generation for da Vinci-like surgical robotic systems," in *Proc. Des. Med. Devices Conf.*, 2018, Art. no. V001T07A008.

[18] S. Sen, A. Garg, D. V. Gealy, S. McKinley, Y. Jen, and K. Goldberg, "Automating multi-throw multilateral surgical suturing with a mechanical needle guide and sequential convex optimization," in *Proc. IEEE Int. Conf. Robot. Autom.*, 2016, pp. 4178–4185.

[19] C. Staub, T. Osa, A. Knoll, and R. Bauernschmitt, "Automation of tissue piercing using circular needles and vision guidance for computer aided laparoscopic surgery," in *Proc. IEEE Int. Conf. Robot. Autom.*, 2010, pp. 4585–4590.

[20] S. Iyer, T. Looi, and J. Drake, "A single arm, single camera system for automated suturing," in *Proc. IEEE Int. Conf. Robot. Autom.*, 2013, pp. 239–244.

[21] F. Nageotte, P. Zanne, C. Doignon, and M. De Mathelin, "Stitching planning in laparoscopic surgery: Towards robot-assisted suturing," *Int. J. Robot. Res.*, vol. 28, no. 10, pp. 1303–1321, 2009.

[22] F. Nageotte, P. Zanne, C. Doignon, and M. DeMathelin, "Visual servoing-based endoscopic path following for robot-assisted laparoscopic surgery," in *Proc. IEEE/RSJ Int. Conf. Intell. Robot. Syst.*, 2006, pp. 2364–2369.

[23] R. C. Jackson and M. C. Çavuşoğlu, "Needle path planning for autonomous robotic surgical suturing," in *Proc. IEEE Int. Conf. Robot. Autom.*, 2013, pp. 1669–1675.

[24] S. Leonard, K. L. Wu, Y. Kim, A. Krieger, and P. C. Kim, "Smart tissue anastomosis robot (STAR): A vision-guided robotics system for laparoscopic suturing," *IEEE Trans. Biomed. Eng.*, vol. 61, no. 4, pp. 1305–1317, Apr. 2014.

[25] B. Huang, M. Ye, Y. Hu, A. Vandini, S.-L. Lee, and G.-Z. Yang, "A multirobot cooperation framework for sewing personalized stent grafts," *IEEE Trans. Ind. Inform*, vol. 14, no. 4, pp. 1776–1785, Apr. 2018.

[26] Y. Hu, L. Zhang, W. Li, and G.-Z. Yang, "Robotic sewing and knot tying for personalized stent graft manufacturing," in *Proc. IEEE/RSJ Int. Conf. Intell. Robot. Syst.*, 2018, pp. 754–760.

[27] S. A. Pedram, P. Ferguson, J. Ma, E. Dutson, and J. Rosen, "Autonomous suturing via surgical robot: An algorithm for optimal selection of needle diameter, shape, and path," in *Proc. IEEE Int. Conf. Robot. Autom.*, 2017, pp. 2391–2398.

[28] A. Guni, N. Raison, B. Challacombe, S. Khan, P. Dasgupta, and K. Ahmed, "Development of a technical checklist for the assessment of suturing in robotic surgery," *Surg. Endoscopy*, vol. 32, pp. 4402–4407, 2018.

[29] J. Ding and N. Simaan, "Choice of handedness and automated suturing for anthropomorphic dual-arm surgical robots," *Robotica*, vol. 33, no. 8, pp. 1775–1793, 2015.

[30] D. A. Sherris and E. B. Kern, *Essential Surgical Skills*. Philadelphia, PA, USA: WB Saunders Company, 2004.

[31] B. K. Horn, "Closed-form solution of absolute orientation using unit quaternions," *J. Opt. Soc. Amer. A*, vol. 4, no. 4, pp. 629–642, 1987.

[32] F. Zhong, Y. Wang, Z. Wang, and Y.-H. Liu, "Dual-arm robotic needle insertion with active tissue deformation for autonomous suturing," *IEEE Robot. Autom. Lett.*, vol. 4, no. 3, pp. 2669–2676, Jul. 2019.

[33] G. Bradski, "The OpenCV Library," *Dr. Dobb's J. Software Tools*, vol. 25, pp. 122–125, 2000.

[34] J. Mattingley and S. Boyd, "CVXGEN: A code generator for embedded convex optimization," *Optim. Eng.*, vol. 13, no. 1, pp. 1–27, 2012.

[35] J. Mahler *et al.*, "Learning accurate kinematic control of cable-driven surgical robots using data cleaning and Gaussian process regression," in *Proc. IEEE Int. Conf. Autom. Sci. Eng.*, 2014, pp. 532–539.

[36] C. D'Ettorre *et al.*, "Automated pick-up of suturing needles for robotic surgical assistance," in *Proc. IEEE Int. Conf. Robot. Autom.*, 2018, pp. 1370–1377.

[37] R. C. Jackson, R. Yuan, D.-L. Chow, W. S. Newman, and M. C. Çavuşoğlu, "Real-time visual tracking of dynamic surgical suture threads," *IEEE Trans. Autom. Sci. Eng.*, vol. 15, no. 3, pp. 1078–1090, Jul. 2018.

[38] B. Lu, X. Yu, J. Lai, K. Huang, K. C. Chan, and H. K. Chu, "A learning approach for suture thread detection with feature enhancement and segmentation for 3-D shape reconstruction," *IEEE Trans. Autom. Sci. Eng.*, vol. 17, no. 2, pp. 858–870, Apr. 2020.

Sahba Aghajani Pedram (Member, IEEE) received the B.S. degree from Sharif University of Technology, Tehran, Iran, in 2012, the M.S. degree from the University of Hawai'i at Manoa, Honolulu, HI, USA, in 2016, and the M.S. and Ph.D. degrees from the University of California at Los Angeles, Los Angeles, CA, USA, in 2018 and 2020, respectively, all in mechanical engineering.

His research interests include medical robotics, estimation, control systems, computer vision, and machine learning.

Changyeob Shin (Member, IEEE) received the B.E. degree in electrical engineering and the M.E. degree in mechanical engineering from Korea University, Seoul, South Korea, in 2013 and 2015, respectively, and the Ph.D. degree in mechanical engineering from the University of California, Los Angeles, Los Angeles, CA, USA, in 2020.

His research interests include robotics, controls, machine learning, and computer vision for automation and human–robot collaboration.

Erik P. Dutson received the M.D. degree and trained in general surgery from Eastern Virginia Medical School, Norfolk, VA, USA, in 1995 and 2000, respectively.

He was further trained in Advanced Laparoscopy, University of Louis Pasteur, Strasbourg, France, in 2003. He is currently an Executive Director of the Center for Advanced Surgical and Interventional Technology, Los Angeles, CA, USA. He is also a Professor of Surgery in the UCLA School of Medicine, Los Angeles, CA, USA.

Peter Walker Ferguson (Graduate Student Member, IEEE) received the B.S. degree in electrical engineering from Loyola Marymount University, Los Angeles, CA, USA, in 2012, and the M.S. degree in mechanical engineering from the University of California, Los Angeles (UCLA), Los Angeles, in 2017.

He is currently a Ph.D. student in mechanical engineering with UCLA. His research interests include wearable robotics, rehabilitation robotics, medical robotics, and mechanical and electrical designs.

Jacob Rosen (Member, IEEE) received the B.Sc. degree in mechanical engineering and the M.Sc. and Ph.D. degrees in biomedical engineering from Tel-Aviv University, Tel-Aviv, Israel, in 1987, 1993, and 1997, respectively.

He is currently a Professor with the Department of Mechanical and Aerospace Engineering and the Director of the Bionics Lab, University of California, Los Angeles, Los Angeles, CA, USA. His research interests focus on medical robotics, biorobotics, human-centered robotics, surgical robotics, wearable robotics, rehabilitation robotics, and neural control.

Ji Ma received the B.S. degree in industrial electrical automation from Shenyang Jianzhu University, Shenyang, China, in 1996, the M.S. degree in control theory and engineering from Northeastern University, Shenyang, China, in 1999, and the Ph.D. degree in mechanical engineering from the University of Hawai'i, Honolulu, HI, USA, in 2009.

He was an Automation Engineer (1999–2001), an Underwater Robotics Engineer (2001–2004), and a Researcher on medical robotics (2005–present). He is currently a Medical Robotics Researcher with the University of California, Los Angeles, Los Angeles, CA, USA. His research interests focus on medical robotics, rehabilitation robotics, haptics, and virtual reality (VR) simulation.